

## RESEARCH ARTICLE

# Modeling the intra-urban nocturnal summertime air temperature fields at a daily basis in a city with complex topography

Moritz Burger<sup>1,2\*</sup>, Moritz Gubler<sup>1,2,3</sup>, Stefan Brönnimann<sup>1,2</sup>

**1** Oeschger Centre for Climate change Research, University of Bern, Bern, Switzerland, **2** Institute of Geography, University of Bern, Bern, Switzerland, **3** Institute for Lower Secondary Education, Bern University of Teacher Education, Bern, Switzerland

\* [moritz.burger@giub.unibe.ch](mailto:moritz.burger@giub.unibe.ch)



## Abstract

Detailed knowledge about the intra-urban air temperature variability within a city is crucial for the implementation of adaptation strategies to counteract the negative effects of urban heat stress. Various methods to model urban-rural temperature differences exist, but they often only cover certain periods (heatwave, hot day) or meteorological conditions (sunny and calm) due to computational limitations or limited data availability. Here, we present a land use regression approach to model nocturnal air temperature fields for every single night of the summers 2018 to 2020 in a city with complex terrain (Bern, Switzerland). Furthermore, we investigate the applicability of different model structures and straight-forward computable GIS variables to model cold air drainage, which exerts an important influence on the local-scale climate of cities with complex terrain. The geostatistical models are calibrated with in-situ data of a dense low cost air temperature measurement network and high resolution spatiotemporal (land use and meteorology) data, which are all publicly available. The resulting land use regression models are capable to model and map intra-urban air temperature differences with a good model performance ( $R^2$ : 0.65–0.71; RMSE: 0.69–0.76 K). Evaluations with data from additional measurement stations and periods (summer 2021) show that the models are able to estimate different meteorological and spatial conditions, but that the representation of small-scale topographic features remains difficult. However, the comparatively low computational and financial effort needed to calculate nocturnal air temperature fields at daily basis enable new applications for cities with restricted resources for various areas of interest, such as urban planning (e.g. effect of heat mitigation policies) or heat risk management (e.g. analyze small-scale urban heat vulnerability).

## OPEN ACCESS

**Citation:** Burger M, Gubler M, Brönnimann S (2022) Modeling the intra-urban nocturnal summertime air temperature fields at a daily basis in a city with complex topography. PLOS Clim 1(12): e0000089. <https://doi.org/10.1371/journal.pclm.0000089>

**Editor:** Jun Yang, Northeastern University (Shenyang China), CHINA

**Received:** May 18, 2022

**Accepted:** October 15, 2022

**Published:** December 5, 2022

**Peer Review History:** PLOS recognizes the benefits of transparency in the peer review process; therefore, we enable the publication of all of the content of peer review and author responses alongside final, published articles. The editorial history of this article is available here: <https://doi.org/10.1371/journal.pclm.0000089>

**Copyright:** © 2022 Burger et al. This is an open access article distributed under the terms of the [Creative Commons Attribution License](https://creativecommons.org/licenses/by/4.0/), which permits unrestricted use, distribution, and reproduction in any medium, provided the original author and source are credited.

**Data Availability Statement:** The raw data of the urban air temperature measurement network used including the metadata can be downloaded from: <https://boris.unibe.ch/161882>.

## Introduction

Mean summer air temperatures as well as the likelihood for air temperature extremes such as very hot days ( $T_{\max} \geq 35^{\circ}\text{C}$ ) and tropical nights ( $T_{\min} \geq 20^{\circ}\text{C}$ ) are increasing across Europe due to the ongoing anthropogenic warming [1,2]. Cities are particularly prone to this shift in

**Funding:** This project is funded by a grant of the Oeschger Centre for Climate Change Research (OCCR), which was endowed to SB. Additionally, since the summer 2021, the measurement network of Bern is funded by the city of Bern and the energy supplier Energie Wasser Bern. The funders had no role in study design, data collection and analysis, decision to publish, or preparation of the manuscript.

**Competing interests:** The authors have declared that no competing interests exist.

summer air temperatures due to the so-called urban heat island (UHI) effect which leads to excess temperatures in urban environments [3], especially during night [4]. The UHI effect is mainly caused by high heat capacities of the used construction material, large fractions of impervious surfaces, low albedos due to the rather dark surfaces and a lack of vegetation and ventilation [3]. Since various negative impacts for cities regarding public health (e.g. increased fatigue, cardiovascular problems), environment (e.g. increased vulnerability of urban trees) or economy (e.g. cooling costs, reduced productivity of people) may arise from urban heat excesses, adaptation strategies to counteract UHIs should be implemented [5].

To plan and implement adequate adaptation measures, detailed knowledge about the air temperature distribution within a city is crucial. Since observational networks in urban environments imply relatively high costs [6] and national weather services typically do not maintain measurement stations within the city [7] different methods to assess and map urban temperatures have been applied in the recent past. The most widespread approaches include satellite-based land surface temperature analyses (which is not comparable with air temperature since the UHI effect is the largest during the day; e.g. [8,9]), numerical urban climate model simulations (e.g. [10,11]), or analyses based on self-designed urban air temperature measurement networks (e.g. [12–14]). Often, only limited timespans with homogeneous synoptic conditions favoring large UHI intensities (e.g. hot days or heatwaves) are investigated due computational limitations (e.g. process based numerical urban climate models) or limited data availability (e.g. satellite images with clouds). However, for several applications such as the assessment of heat risk for the urban populations (e.g. [15]) or the planning of UHI mitigation strategies (e.g. [16]), timespans also covering a variety of synoptic conditions are needed. Additionally, extended modeling periods would also enable the possibility to calculate and investigate threshold statistics such as the number of tropical nights in a specific neighborhood.

The combination of in-situ data from a low cost urban air temperature measurement network with publicly available spatial data offers the opportunity of conducting daily models and maps of entire summer periods with geostatistic land use regression (LUR) models with relatively low computational and financial effort [17]. Since the formation and the magnitude of the UHI effect depends to a large extent on meteorological preconditions [18], it is crucial to incorporate meteorological variables, if a larger timespan is analyzed [4,17]. Many studies have been conducted using meteorological variables as predictors of UHI intensities, of which wind speed and cloud cover (solar radiation) were often identified as the meteorological variables having the greatest impact on the UHI [4,18–21]. In addition, other variables such as relative humidity [20,21] or daily temperature range [4] were identified as predicting variables. Precipitation is rarely investigated, since many studies focus on weather conditions that exacerbate urban heat, which implies that days with precipitation are often excluded from the analyses [4,14], although the reducing effect of precipitation on the UHI intensity is evident [22].

In addition to meteorological and land use patterns, cold air drainage (CAD) might be another important factor shaping the air temperature distribution within a city [23,24]. Such cooling airflow systems at local scales are mainly caused by drainage due to hilly terrain [25] and depend on the interaction of such topographical features and urban morphology. In existing LUR studies, such specific cold air variables are often not incorporated (e.g. [4,26,27]) or the focus is set on ventilation paths (e.g. with the proxy front area index, [28,29]) which do not account for CAD caused by terrain features, since the spatial connectivity between cold-air source areas (production) and urban areas (impact) is not considered [24]. However, approaches to model topographic proxies for CAD exist and can be grouped in two categories: First, flow accumulation proxies that take into account that cold air is denser than warm air and that thus the flow and accumulation of cool air parcels can be modeled similar to water

[17,30]. Second, relative elevation proxies that compare the position (elevation) of a grid cell with the surrounding grid cells and expect cool air to accumulate in concave landforms [31–34]. However, some of those studies were conducted in the field of ecology focusing on environmental conditions outside of urban environments [30–33]. The applicability of those proxies in urban environments has thus received limited attention and comparisons between the different approaches are lacking.

The aim of this study is to model nocturnal UHI intensities and map summertime nighttime air temperatures of Bern, Switzerland for every night during the summers 2018 to 2020, using a LUR approach that combines publicly available land use and meteorological data. Based on data of a dense urban measurement network [35] and previous LUR models [17], we expand the models from heatwave means to daily fields and evaluate different model structures and CAD variables to estimate the nocturnal air temperature variability in a city with complex topography.

## Data and methods

### Study site

With 134'000 inhabitants, Bern is a medium-sized city in Switzerland [36]. The city is located in the mid-Western part of the Swiss Plateau at a mean elevation of 550 m.a.s.l. and is characterized by its complex topography: Several hills, including two which reach more than 850 m. a.s.l. in the northeast (Bantiger, 947 m.a.s.l.) and in the south (Gurten, 858 m.a.s.l.), various depressions, and a river (Aare) shape the natural topography of Bern and its surroundings [23] (Fig 1). Important regional effects of the complex topography are air temperature inversions with different thickness layers that evolve in summer during every second night [37] and the canalization of the wind due to the blocking of the nearby mountain ranges Jura and Alps which leads to a domination of southwestern and northeastern wind systems [23] (Fig 1A). During calm nights, also weak katabatic winds from southeast occur [23]. Bern experiences warm humid summers with a mean summer air temperature of 17.4°C and a mean summer precipitation amount of 333 mm throughout the climatological reference period 1980–2010 [38].

### Data

**Urban air temperature data.** From 2018 to 2021, a dense urban air temperature measurement network is operated in the city of Bern throughout summertime. It consists of 70 to 90 stations, which are installed from mid-May to mid-September and record the air temperature at an interval of 10 min. The stations are mounted at a height of approximately 3 m at free-standing poles and cover the microclimatic and topographic heterogeneity of the city. Even though the stations consist of low cost devices (about 65 CHF per station) and are only passively ventilated, they are able to capture nighttime temperatures (22 pm to 6 am) with only small biases when compared to professional actively ventilated sensors (mean bias: -0.12 to 0.23 K, [35]). During daytime, a mean positive bias of 0.61 to 0.93 K is observed, which implies that the uncertainties due to the measurement devices might be larger than the observed daytime urban heat island [17,35]. Due to these constraints, we focus on the nocturnal temperature data in this study. Hence, for the calibration of the models, we use mean nighttime temperatures (22 pm to 6 am) of 61 stations that were placed at the same location from 2018 until 2020 (276 days; Fig 1B). Data from 17 additional stations in 2018 as well as data of the remaining 55 calibration station in summer 2021 is used for the evaluation (92 days each).

**Meteorological reference data.** The official measurement station in Bern maintained by the Federal Office of Meteorology and Climatology (Meteoswiss) is located about 5 km north



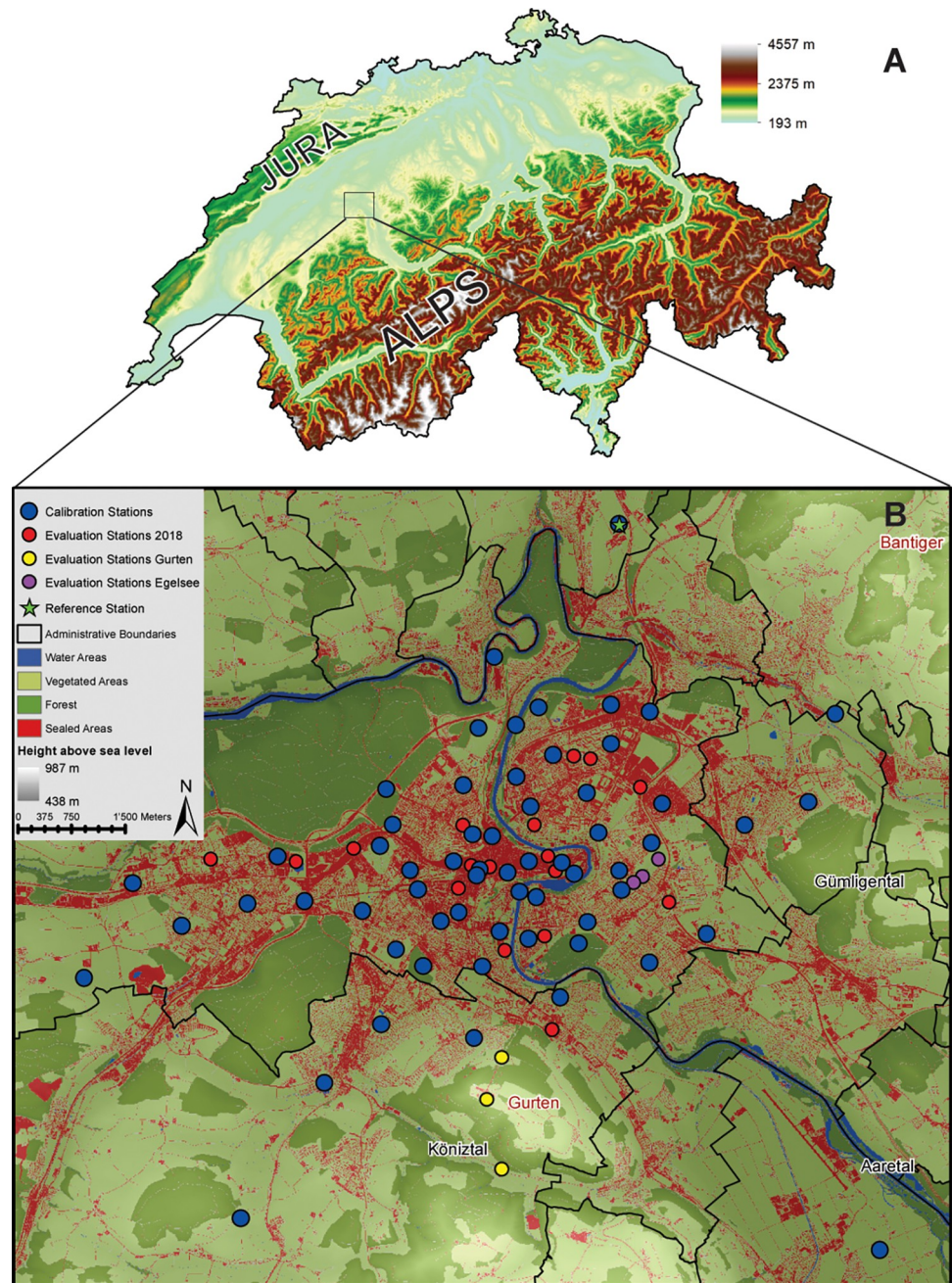


**Fig 1.** Overview on the location of the study area (A) with the main topographical features of Switzerland and the study area's detailed topography (bright / dark), land cover, and air temperature measurement locations (B). Blue dots represent the 61 calibration stations and red dots the 17 evaluation stations of 2018. The yellow (Gurten hill, mounted in 2021) and purple (Egelsee depression, mounted in 2019) dots represent the evaluation stations over complex terrain. Additionally indicated are the most important valleys and hills in the surroundings of Bern. The base layers can be downloaded using the following links <https://www.swisstopo.admin.ch/en/geodata/height/alti3d.html> (topography) and <https://geoportal14.laborplatz.ch/de/geodaten/geoproduktedownload/listing/display?type=geoprodukt&code=MOPUBE> (land use).

<https://doi.org/10.1371/journal.pclm.0000089.g001>

**Table 1. Temporal and spatial variables tested in this study with their abbreviations, chosen buffer widths and units as well as their data source and available resolution.**

Variable	Abbreviation	Chosen Buffer Width (m)	Unit	Data Source	Resolution
<b>Temporal Variables</b>					
Global Solar Radiation	G	-	Wm <sup>-2</sup>	[40]	10 min
Precipitation	RR	-	mm	[40]	10 min
Relative Humidity	RH	-	%	[40]	10 min
Wind Speed	FF	-	ms <sup>-1</sup>	[40]	10 min
Wind Direction	DD	-	°	[40]	10 min
<b>Spatial Variables—Land Cover</b>					
Buildings	B	250	%	[41]	- (vector data)
Open Space Sealed	SE	1000	%	[41]	- (vector data)
Open Space Garden	GA	25	%	[41]	- (vector data)
Open Space Agriculture	AC	750	%	[41]	- (vector data)
Open Space Forest	FO	1000	%	[41]	- (vector data)
Open Space Water	WA	150	%	[41]	- (vector data)
<b>Spatial Variables -Topography</b>					
Altitude Difference	AD	-	m	[42]	2 m
Slope	SLO	50	°	[42]	2 m
Northness	NOR	100	0 to 1	[42]	2 m
<b>Spatial Variables—Vegetation</b>					
Amount of Trees	AMT	100	Count	[43]	- (vector data)
Vegetation Height	VH	150	m	[44]	1 m
<b>Spatial Variables—Urban Surface Geometry</b>					
Mean Building Height	MBH	150	m	[45]	- (vector data)
Building Volume Density	BVD	500	m	[45]	- (vector data)
Sky View Factor	SVF	50	0 to 1	[42,44,45]	5 m
<b>Spatial Variables—Cold Air Drainage</b>					
Flow Accumulation	FA	100	Number	[42]	2 m
Flow Accumulation with Buildings	FAB	100	Number	[42,44,45]	5 m
Relative Height	REH	500	Number	[42]	2 m
Topographic Position Index	TPI	500	Number	[42]	2 m

<https://doi.org/10.1371/journal.pclm.0000089.t001>

of the city center in Zollikofen at an elevation of 553 m.a.s.l. (Fig 1B). It is a WMO-certified station, which should per definition not be influenced by urban heat [39]. Out of the 12 different meteorological variables recorded, we use air temperature at two meters as the basis temperature for the models as well as relative humidity, precipitation, global solar radiation and wind speed and wind direction as explanatory variables (Table 1), which are averaged over a 24 h (6 am to 6 am) and a nighttime 8 h interval (22 pm to 6 am). The data is publicly available and can be downloaded on the website of Meteoswiss [40].

**Land use variables.** In order to model the influence of the land use on the urban nighttime air temperatures, 14 land use and 4 additional CAD variables were calculated (Table 1), which are shortly described in the following. For more detailed information about the computation of the land use variables, see [17].

Six land cover parameters were derived from the cantonal cadastral survey [41]: Buildings [BUL], Open Space Sealed [SE], Open Space Garden [GA], Open Space Agriculture [AC], Open Space Forest [FO] and Open Space Water [WA]. Geospatial information regarding topography were derived from a high-precision digital elevation model [42] (Slope [SLO], Northness [NOR]). Moreover, the difference in altitude from a location to the reference station

(Altitude Difference [AD]) was also derived from that dataset. Detailed information about vegetation parameters were derived from a topographic landscape model [43] (Amount of Trees [AMT]) and from the Swiss Federal Research Institute WSL [44] (Vegetation Height [VH]). Finally, information about the urban surface geometry (buildings) was gained from the swiss-BUIDINGS<sup>3D</sup> 2.0 dataset [45] (Mean Building Height [MBH], Building Volume Density [BVD] and Sky View Factor [SVF]).

**Cold air drainage variables.** In total four different CAD variables of two different groups were derived. The first group was calculated with the commands “flow direction” and “flow accumulation” in ArcGis (version 10.7.1) [46] using a high-precision digital elevation model (DEM) of Bern [42]. With these features, the flow from a cell of a raster to its neighboring cells is calculated (according to the height of the cell) and then accumulated over the entire area. This approach was originally developed for hydrological analyses [47]. Applied to CAD, it follows the idea that cold air behaves similar than water: cool dense air follows the topography [33] and accumulates in the steepest descents [30]. This method was already tested for Bern in an earlier study. Although it worked well in the model evaluation, the amplitude of cooling appeared to be overestimated at some non-monitored locations when mapping it [17]. In this study, different DEM resolutions (25 to 250 m) were tested and logarithmic variables were calculated. One of the variables is calculated using a DEM (Flow Accumulation; FA) and one with buildings and vegetation placed on the DEM (Flow Accumulation with buildings; FAB) (Table 1). This method implies that the buildings block CAD, but has the disadvantage that CAD may also form at the rooftops of buildings.

The second group of CAD variables was calculated based on comparisons of the elevation of a grid cell with its neighboring cells. The first approach compares the elevation of a site with the minimum elevation within a specified radius in order to distinguish locations where air would drain away (high value) or cold air could pool (low value). This so called “Relative Height” REH is the third CAD variable used here and has been tested in earlier studies [31,32]. If not the minimum, but the mean elevation of the surrounding grid cells is subtracted from a grid cell, the “Topographic Position Index” (TPI) is calculated [34]. Negative TPI values indicate concave positions (valley) where cold air drainage is favored, positive TPI values indicate convex positions (hilltop) where no cold air drainage is expected. TPI is the fourth CAD variable tested in this study.

**Buffer zone radii.** In LUR, temperatures at a specific location are expressed as functions of land use characteristics in circular areas surrounding the location (buffers). Depending on the land use variable, the radius of that area is chosen differently [48]. Here, we tested buffer radii values from 25 to 1000 m. The selection of the best fitting buffer zone radii per land use variable was conducted with linear regression modeling (see [17] for detailed description, Table 1).

**Model structure.** The study aims to develop spatiotemporal geostatistical models for estimating the nighttime (22 pm to 6 am) air temperature fields in Bern with the antecedent mentioned data. We use the mean air temperature difference of a station of the urban network to the reference station in Zollikofen as the response variable of the model. Although the definition of stations to be “rural” and “urban” is problematic and hence the use of term “UHI intensity” not fully appropriate [49], we use that term for these air temperature differences due to simplicity reasons. To calculate absolute nighttime air temperature fields, we add the observed mean nighttime air temperature of Zollikofen to the modelled UHI intensities.

As first step of the modeling process, we analyze the independent influence of meteorology and land use on the UHI intensity to decide upon which variables are used for the further modeling. Whereas the investigation of the meteorological variables is important for the estimation of potential UHI intensity in general (e.g. strong UHI intensity expected after a sunny

**Table 2. The different model structures.**

ADD	$T_{Sji} - T_{Zi} = \left( \sum_{t=1}^n a_t \times M_{ti} \right) + \left( \sum_{s=1}^m b_s \times L_{sj} \right)$
MULT	$T_{Sji} - T_{Zi} = \left( \sum_{t=1}^n a_t \times M_{ti} \right) \times \left( \sum_{s=1}^m b_s \times L_{sj} \right)$
INT	$T_{Sji} - T_{Zi} = \left( \sum_{t=1}^n a_t \times M_{ti} \right) + \left( \sum_{s=1}^m b_s \times L_{sj} \right) + \left( \sum_{t=1}^n \sum_{s=1}^m c_{ts} \times (M_{ti} \times L_{sj}) \right)$

$T_{Sji}$  represents the observed air temperature at station  $j$  of the urban temperature network for the night  $i$ .  $T_Z$  represents the observed nighttime air temperature at the reference station in Zollikofen.  $M$  denotes the temporal and  $L$  the spatial variables of whom  $n$  and  $m$  exist.  $a_t$  represents the slopes of the temporal,  $b_s$  the slopes of the spatial and  $c_q$  the slopes of the combined predictors.

<https://doi.org/10.1371/journal.pclm.0000089.t002>

day and a calm, dry night), the land use variables are used to estimate the urban heterogeneity and intra-urban distribution of temperature. As second step, three different model structures to combine meteorological and land use variables are tested: First, we build an additive model (ADD; Table 2), where meteorological and land use variables are combined with a multiple linear regression (MLR) model similarly to the approach of [28] applied to Hongkong. Second, a two-step multiplicative structure is tested (MULT, Table 2) according to the diagnostic UHI equation model for cities in northwestern Europe [4]. Here, a meteorological MLR model is first fitted, independently from the land use variables. Based on that meteorological model, a best fit of constant is calculated for every station, based on the mean absolute error in order to get the equation “constant  $\times$  meteorological model”. As a last step, another MLR is conducted to represent the constant with land use variables that will have been selected in the previous chapter [4]. As a third model structure, we test a novel approach of an interactive model structure (INT, Table 2). The idea of that approach is that possible interactions between meteorology and land use variables are considered [50]. Non-significant interaction pairs ( $p > 0.001$ ) are omitted from the model. Although the computation of the model is rather simple, the structure gets more complicated (Table 2).

## Mapping

To illustrate the outputs of the different LUR models, we map the modeled air temperatures with a 50 m  $\times$  50 m resolution for the greater area of Bern using R [51]. We show the predicted air temperature distribution of two meteorologically different nights with conditions favoring and hindering strong UHI intensities.

## Evaluation

To evaluate the models, additional station data is used. We use data from 17 additional stations that were only installed during summer 2018 (Fig 1B) as well as data of the remaining calibration stations that were installed during summer 2021 (55 out of 61). Explained variance ( $R^2$ ), root mean square error (RMSE) and mean bias (MB) are calculated in order to assess the performance of the models. Additionally, we compare the ability of the different models to predict



nighttime air temperatures over complex topographical features with additional data from three locations at the Gurten hill south of the city at elevations of 848, 694 and 631 m.a.s.l. mounted in summer 2021, as well as with data from three stations which were mounted during summer 2019 in a small-scale topographic depression within the built up area (“Egelsee”) in the east of the city (Fig 1B).

## Results

### Independent selection of meteorological and land use variables

**Meteorology.** For this analysis, the mean nighttime UHI intensity per day of all 61 stations is calculated ( $n = 276$ ) and compared with the corresponding value of the meteorological variables (Fig 2). A positive correlation of global solar radiation ( $r = 0.58$ ; Fig 2A) and UHI intensity, as well as negative relations between precipitation and UHI intensity ( $r = -0.47$ ; Fig 2B) and relative humidity and UHI intensity ( $r = -0.49$ ; Fig 2D) can be observed. The influence of wind is less evident, a slight increase in UHI intensity with stronger wind is found ( $r = 0.06$ ; Fig 2C).

Further analyses on the wind showed the important role of the wind direction. Enhanced winds from north (average between  $270$  and  $90^\circ$ ) is associated with an increase of the UHI intensity ( $r = 0.41$ ), while winds from south result in a decrease ( $r = -0.63$ ). This feature is the most prominent if nighttime winds are analyzed (Fig 2E). Subsequent analysis on precipitation showed that the occurrence of precipitation itself is more important than the actual amount and that nighttime precipitation shows a stronger relationship with the UHI intensity than 24-hour precipitation (Fig 2F).

With the variables mentioned above, MLR modeling was conducted. The results showed that global solar radiation, winds from South (SWI), relative humidity and the Boolean

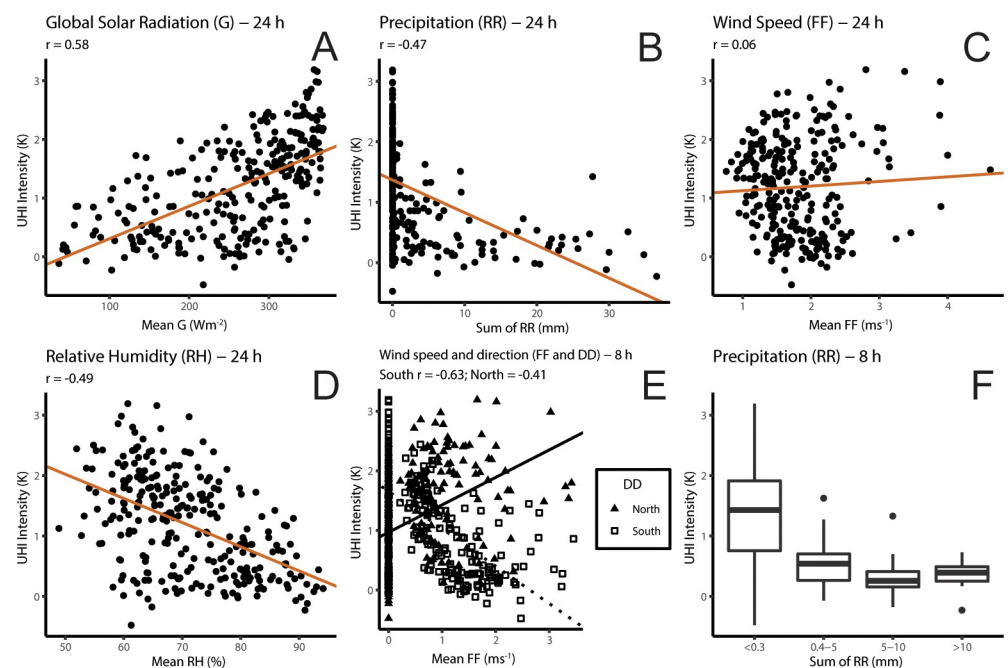


**Fig 2.** Linear regressions of meteorological variables and the mean UHI intensity per day (A-E) and the influence of the amount of precipitation on the UHI intensity (F). The lines represent the linear regressions and  $r$  the strength of the correlation (A-E).

<https://doi.org/10.1371/journal.pclm.0000089.g002>



**Table 3. Structure of the independent meteorological (MET) and the land use models with the four different CAD proxies tested (FA, FAB, TPI and REH; first step of the modeling process).** Indicated are the number of observation of each model (n) and the corresponding  $R^2$  and RMSE values. SWI stands for winds from south and NR for the Boolean nighttime precipitation variable. YES means it rained and the value is 1, otherwise it is 0.

Model	Structure	n	$R^2$	RMSE
MET	$0.53 + 0.0043 \times G - 0.519 \times \text{SWI} - 0.479 \times \text{NR (YES)}$	276	0.69	0.45 K
FA	$1.776 + 2.121 \times \text{BUL} - 1.653 \times \text{FO} - 0.644 \times \text{GA} - 2.592 \times \text{AC} - 0.056 \times \text{VH} - 0.211 \times \text{FA} + 0.002 \times \text{AD}$	61	0.87	0.31 K
FAB	$1.834 + 2.160 \times \text{BUL} - 1.784 \times \text{FO} - 0.708 \times \text{GA} - 2.626 \times \text{AC} - 0.058 \times \text{VH} - 0.238 \times \text{FAB} + 0.003 \times \text{AD}$	61	0.86	0.33 K
TPI	$1.777 + 1.820 \times \text{BUL} - 1.840 \times \text{FO} - 0.732 \times \text{GA} - 2.752 \times \text{AC} - 0.061 \times \text{VH} + 0.012 \times \text{TPI} + 0.002 \times \text{AD}$	61	0.86	0.32 K
REH	$1.564 + 1.987 \times \text{BUL} - 1.830 \times \text{FO} - 0.726 \times \text{GA} - 2.744 \times \text{AC} - 0.058 \times \text{VH} + 0.006 \times \text{REH} + 0.002 \times \text{AD}$	61	0.86	0.32 K

<https://doi.org/10.1371/journal.pclm.0000089.t003>

nighttime precipitation variable (Nightrain; NR) had a significant influence on the mean UHI intensity. Since global solar radiation and relative humidity showed a high collinearity, and relative humidity contributed only very little to the explanation of the UHI intensity of the model, it was excluded in the final meteorological model and the subsequent calculations. The final meteorological model explains 69% of the variance of the mean UHI intensity per day with a RMSE of 0.45 K (Table 3, Model “MET”).

**Land use.** For this analysis, the mean UHI intensity per station over the 276 days is calculated ( $n = 61$ ). MLR analyses were conducted for the four models incorporating different CAD variables. However, all models include the same land use variables and the performance is very similar, with  $R^2$  values between 0.86 and 0.87 and RMSEs between 0.31 and 0.32 K (Table 3, Models FA, FAB, TPI, REH).

## Combining meteorology and land use

The combined models reach  $R^2$  values from 0.65 to 0.71 and RMSEs from 0.69 to 0.76 K (Table 4). The performance of the models increase with their complexity, while the differences between the CAD variables remain small (Tables 4 and 5). Irrespective of the model complexity, strongly negative UHI intensities seem to be poorly estimated by all models (Fig 3).

## Mapping the urban air temperature distribution of two different nights

The predicted nighttime air temperatures of two meteorologically diverse nights are compared in order to investigate differences in model performance related to different model structures (Figs 4 and S2–S4) and CAD variables (Figs 5 and S5–S10). Favorable conditions to form large UHI intensities were experienced during the night of the 5<sup>th</sup> of August 2018: After a sunny day ( $G = 304.9 \text{ Wm}^{-2}$ ), a dry and calm ( $FF = 0.73 \text{ ms}^{-1}$ ) night followed, with winds from northeast. While the solar radiation was similar during the day of the 9<sup>th</sup> August of 2019 ( $G = 271.6 \text{ Wm}^{-2}$ ).

**Table 4. Calibration statistics and model performance ( $R^2$  and RMSE) for the combined models (second step of the modeling process).** Three different model structures (ADD, MULT and INT) with four different CAD variables (FA, FAB, TPI and REH) were calibrated with  $m = 61$  stations for  $n = 276$  days.

Model structure	FA		FAB		TPI		REH	
	$R^2$	RMSE	$R^2$	RMSE	$R^2$	RMSE	$R^2$	RMSE
ADD	0.66	0.75 K	0.65	0.76 K	0.65	0.76 K	0.66	0.76 K
MULT	0.67	0.74 K	0.67	0.74 K	0.67	0.74 K	0.67	0.74 K
INT	0.71	0.69 K	0.71	0.69 K	0.71	0.69 K	0.71	0.69 K

<https://doi.org/10.1371/journal.pclm.0000089.t004>

**Table 5. Structure of the combined TPI models (second step of the modeling process).** The models of the other CAD variables can be found in the supplementary material (S1–S3 Tables).

TPI models	Structure
ADD	$1.1 + 1.83 \times \text{BUL} - 1.85 \times \text{FO} - 0.74 \times \text{GA} - 2.76 \times \text{AC} - 0.06 \times \text{VH} + 0.002 \times \text{AD} + 0.01 \times \text{TPI} + 0.004 \times \text{G} - 0.52 \times \text{SWI} - 0.48 \times \text{NR}$
MULT	$(0.53 + 0.004 \times \text{G} - 0.52 \times \text{SWI} - 0.48 \times \text{NR}) \times (1.4 + 1.84 \times \text{BUL} - 1.75 \times \text{FO} - 0.57 \times \text{GA} - 2.05 \times \text{AC} - 0.04 \times \text{VH} + 0.01 \times \text{AD} + 0.01 \times \text{TPI})$
INT	$0.6 + 1.01 \times \text{BUL} - 0.72 \times \text{FO} - 0.29 \times \text{GA} - 0.61 \times \text{AC} - 0.03 \times \text{VH} - 0.001 \times \text{AD} - 0.001 \times \text{TPI} + 0.007 \times \text{G} - 0.49 \times \text{SWI} - 1.0 \times \text{NR} + 0.005 \times (\text{G} \times \text{BUL}) - 0.006 \times (\text{G} \times \text{FO}) - 0.002 \times (\text{G} \times \text{GA}) - 0.01 \times (\text{G} \times \text{AC}) - 0.0001 \times (\text{G} \times \text{VH}) + 0.00005 \times (\text{G} \times \text{AD}) + 0.00006 \times (\text{G} \times \text{TPI}) - 0.48 \times (\text{SWI} \times \text{BUL}) + 0.37 \times (\text{SWI} \times \text{FO}) + 0.35 \times (\text{SWI} \times \text{AC}) - 0.008 (\text{SWI} \times \text{VH}) - 0.001 (\text{SWI} \times \text{AD}) + 1.24 \times (\text{NR} \times \text{FO}) + 0.33 (\text{NR} \times \text{GA}) + 1.63 \times (\text{NR} \times \text{AC}) + 0.02 \times (\text{NR} \times \text{VH}) - 0.006 (\text{NR} \times \text{AD}) - 0.006 (\text{NR} \times \text{TPI})$

<https://doi.org/10.1371/journal.pclm.0000089.t005>

<sup>2</sup>), a cold front reached Switzerland after sunset. It rained in Bern during the night (RR = 11.7 mm), and southwesterly winds reached a mean strength of  $1.89 \text{ ms}^{-1}$ . However, the mean nighttime air temperatures at Zollikofen were similar with  $21.7^\circ\text{C}$  at the 5<sup>th</sup> of August 2018 and  $20.9^\circ\text{C}$  at the 9<sup>th</sup> of August 2019.

While the air temperature distribution and the performance of the models are similar during the night with favorable conditions (Fig 4A, 4C and 4E), differences appear between the model structures for the night with unfavorable conditions to form large UHI intensities (Fig 4B, 4D, and 4F). A strongly pronounced UHI is predicted by the ADD model (Fig 4B), while almost no temperature variability is estimated by the MULT model (Fig 4D). A weak UHI is predicted by the INT model, which results in a better model performance for that night (r: 0.90 compared to 0.80 (ADD) and 0.73 (MULT); Fig 4B, 4D, and 4F).

The predicted nighttime air temperatures of the INT models look very similar for all CAD variables with differences being mostly smaller than 0.5 K (Figs 4, 5 and S2–S10). Larger differences are observed during the night of the 5<sup>th</sup> of August 2018 close to the hills and valleys outside of the city, such as Gurten hill and its adjacent valley in the south (Köniztal; Figs 1B and 5). While the slopes of the hills are estimated to be warmer by the REH model (Fig 5A–5C), the temperatures of

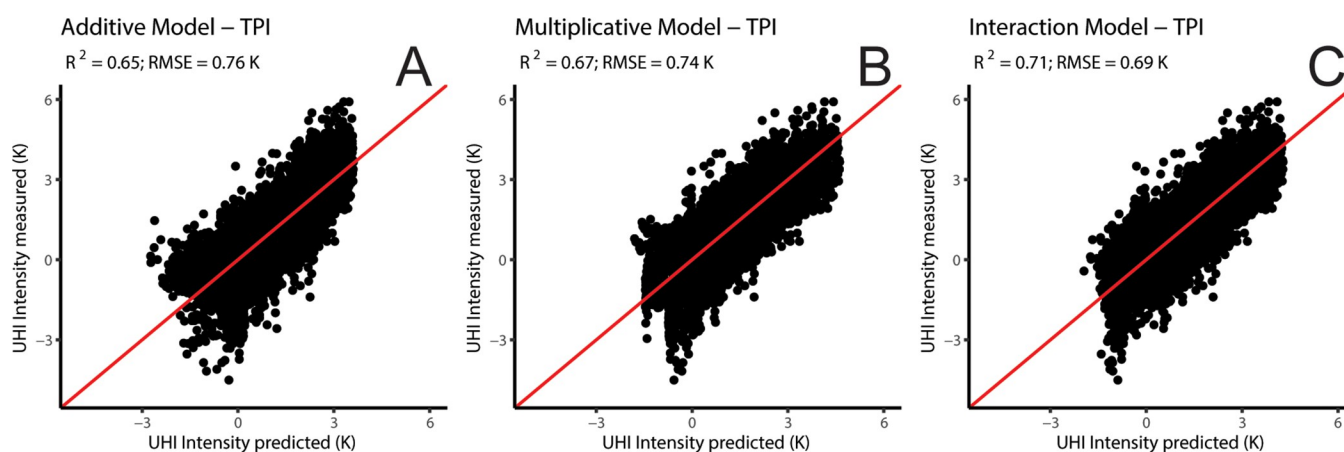


**Fig 3. Predicted (x-axis) versus measured UHI intensities of the three different TPI models.** The plots of the models with the other CAD variables can be found in the supplementary material (S1 Fig).

<https://doi.org/10.1371/journal.pclm.0000089.g003>

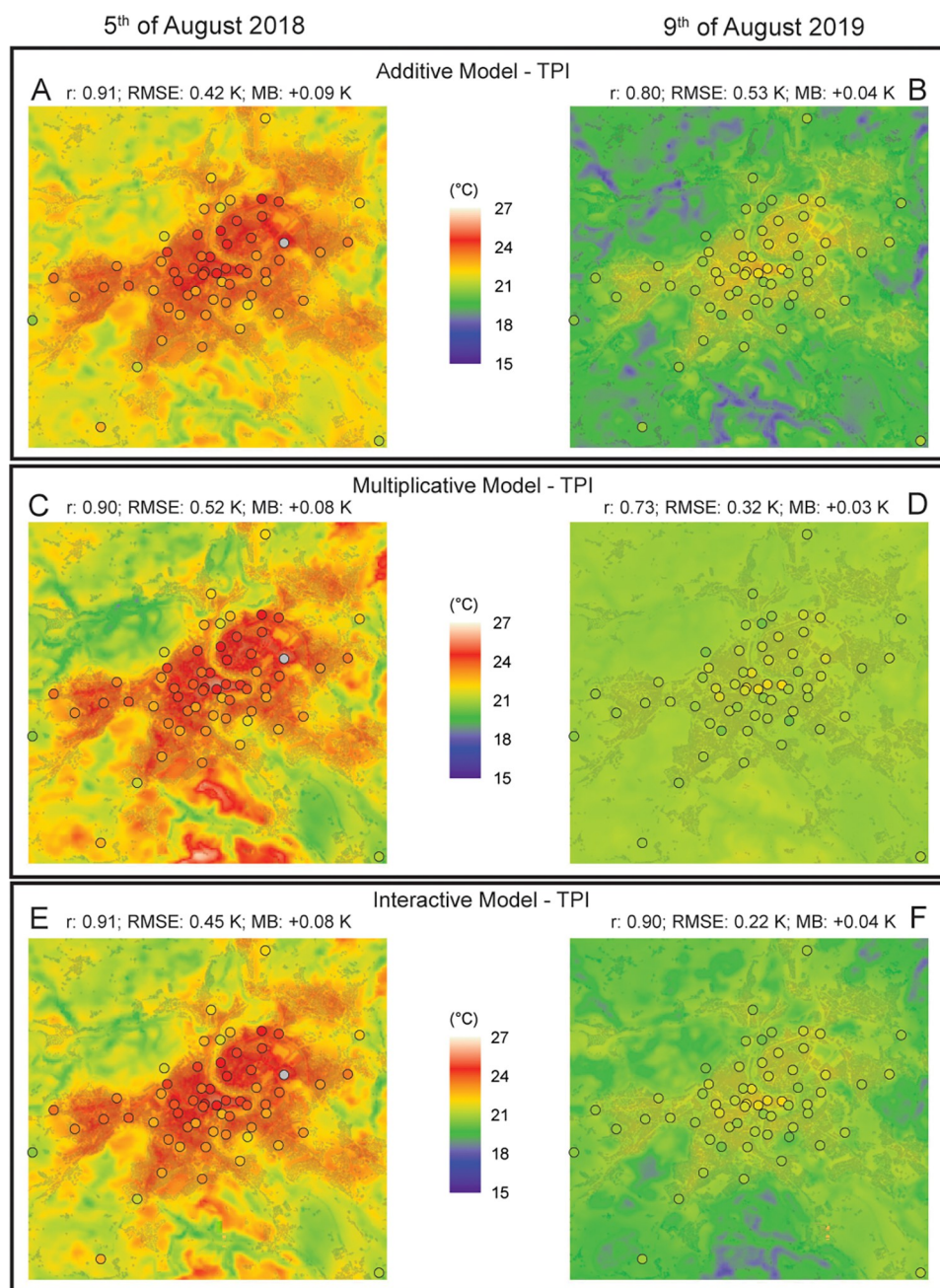


**Fig 4.** Predicted mean nighttime air temperatures derived from the ADD (A and B), MULT (C and D), and INT models (E and F) with the CAD variable TPI for the 5<sup>th</sup> of August 2018 (A, C, and E) and the 9<sup>th</sup> of August 2019 (B, D, and E). The dots show measured mean nighttime air temperatures of the correspondent night at the sites used for the modeling. The model performance is indicated by the correlation ( $r$ ), the root mean square error (RMSE) and the mean bias (MB). The resulting maps of the other CAD variables as well as high resolution maps of the INT models of all CAD variables can be found in the supplementary material (S2–S8 Figs). The base layer (building shadows) can be downloaded using the following link: <https://www.swisstopo.admin.ch/en/geodata/landscape/buildings3d2.html>.

<https://doi.org/10.1371/journal.pclm.0000089.g004>

the valleys (as well as the river) are modeled lower with the TPI model (Fig 5A, 5D and 5E). Several cold air flows are modeled by the flow accumulation based models, resulting in these locations appearing cooler in those models (Fig 5B–5E). However, the performance of all CAD models is virtually the same for the two days mapped and for the calibration period.



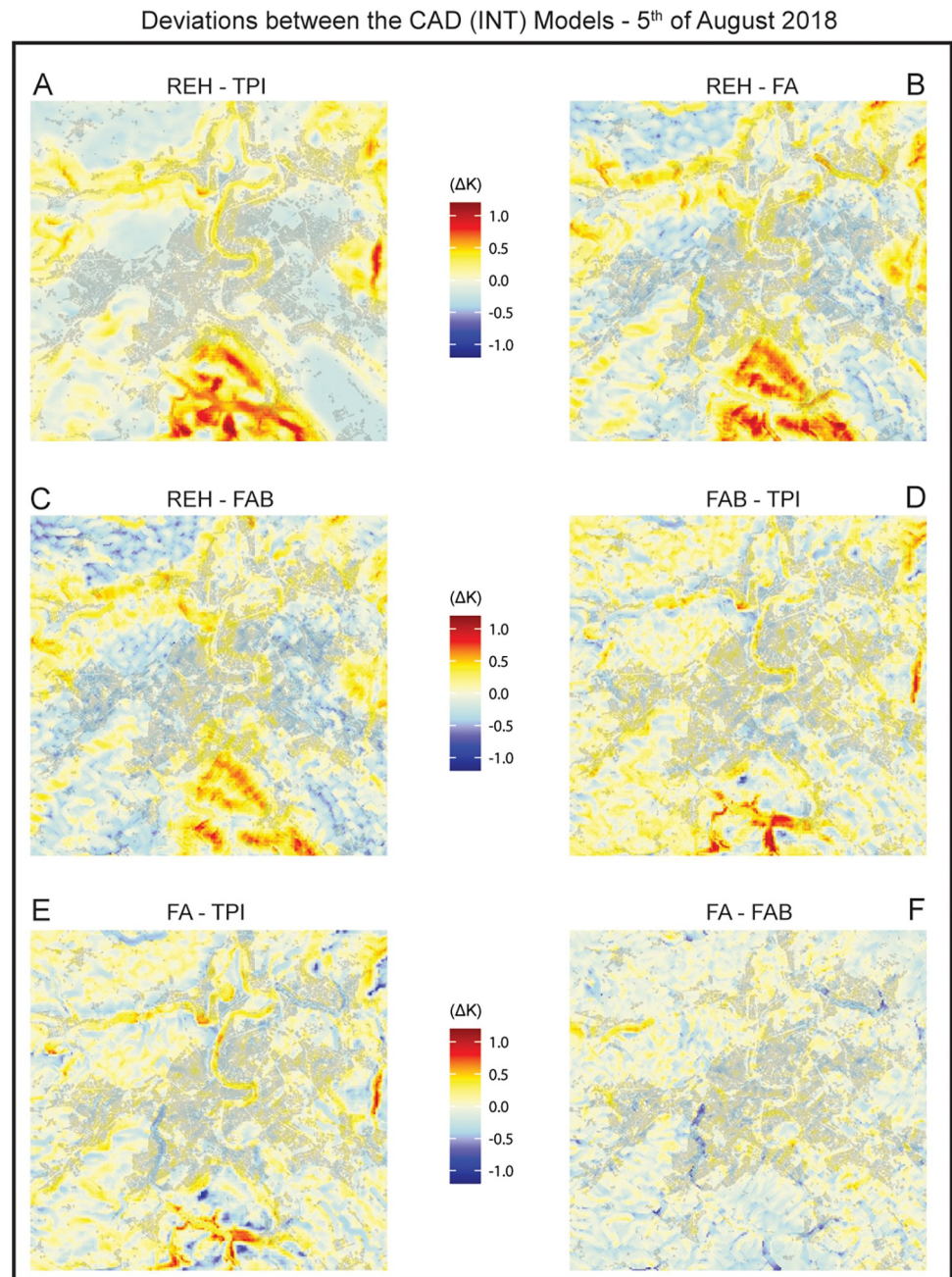


**Fig 5. Deviations in predicted mean nighttime air temperatures between the four different Cold Air Drainage (CAD) Interaction models for the 5<sup>th</sup> of August 2018.** The figure of the 9<sup>th</sup> of August 2019 can be found in the supplementary material (S10 Fig). The abbreviations stands for the different CAD proxies: REH = Relative Height; TPI = Topographic Position Index; FA = Flow Accumulation; FAB = Flow Accumulation with Buildings. The base layer (building shadows) can be downloaded using the following link: <https://www.swisstopo.admin.ch/en/geodata/landscape/buildings3d2.html>.

<https://doi.org/10.1371/journal.pclm.0000089.g005>

## Model evaluation

**Additional stations in 2018.** Applied to the data of the 17 additional stations in 2018, the performance of the models is similar than with the calibration data (Tables 4 and 6). The UHI intensity of these additional stations are in general slightly underestimated (MB: -0.21 to -0.29



**Table 6. Resulting  $R^2$ s, RMSEs and MB of the different model structures and CAD variables for the evaluation with additional data of the summers 2018 ( $n = 92$ ;  $m = 17$ ) and 2021 ( $n = 92$ ;  $m = 55$ ).**

Model structure	FA			FAB			TPI			REH		
	$R^2$	RMSE	MB	$R^2$	RMSE	MB	$R^2$	RMSE	MB	$R^2$	RMSE	MB
Additional stations in 2018												
ADD	0.68	0.83 K	-0.23 K	0.69	0.85 K	-0.26 K	0.69	0.84 K	-0.26 K	0.70	0.84 K	-0.28 K
MULT	0.72	0.76 K	-0.25 K	0.72	0.77 K	-0.27 K	0.72	0.77 K	-0.28 K	0.73	0.76 K	-0.29 K
INT	0.71	0.77 K	-0.21 K	0.71	0.78 K	-0.24 K	0.71	0.78 K	-0.24 K	0.73	0.77 K	-0.26 K
Model station in 2021												
ADD	0.59	0.84 K	+0.43 K	0.59	0.84 K	+0.41 K	0.60	0.84 K	+0.42 K	0.59	0.84 K	+0.42 K
MULT	0.63	0.82 K	+0.42 K	0.63	0.82 K	+0.41 K	0.63	0.81 K	+0.41 K	0.63	0.82 K	+0.43 K
INT	0.67	0.77 K	+0.42 K	0.66	0.77 K	+0.42 K	0.67	0.77 K	+0.42 K	0.67	0.77 K	+0.42 K

<https://doi.org/10.1371/journal.pclm.0000089.t006>

K). The performances of the different model structures are closer together, compared to results of the calibration data.

**Model stations during summer 2021.** Applied to data of the 55 remaining stations in 2021, the model performance is slightly worse compared to the calibration data (Table 4) and the UHI intensities of all stations are overestimated by 0.41 to 0.43 K (Table 6). While the CAD variables lie close to each other, the performance of the model structures increases with increasing complexity.

## Evaluation over small-scale complex topographic features

**Gurten hill 2021 and Egelsee depression 2019.** The evaluation on the three additional stations at Gurten hill in 2021 shows that the air temperatures are (slightly) overestimated by all models. While the positive mean biases and the RMSEs of the MULT models are large, the INT models show the highest  $R^2$ , the lowest RMSEs, and only very small positive mean biases (Table 7). The differences between the CAD proxies are small with REH models showing slightly lower model fits (RMSE 1.12 to 1.88 K compared to 1.02 to 1.74 K).

Applying the LUR models on the additional data at the topographic depression “Egelsee” showed that none of them could adequately represent this small-scale cold air pool, which can reach up to -3 K during favorable conditions. The air temperatures of the three stations are overestimated by more than 1 K on average and the variance could not be explained ( $R^2 = 0.00$ ). All CAD proxies perform similarly poor (Table 7).

**Table 7. Resulting  $R^2$ s, RMSEs and MBs of the different model structures and CAD variables for the evaluation with complex topographic features Gurten hill ( $n = 92$ ;  $m = 3$ ) and Egelsee depression ( $n = 92$ ;  $m = 3$ ).**

Model structure	FA			FAB			TPI			REH		
	$R^2$	RMSE	MB	$R^2$	RMSE	MB	$R^2$	RMSE	MB	$R^2$	RMSE	MB
Gurten hill 2021												
ADD	0.31	1.12 K	+0.11 K	0.31	1.12 K	+0.07 K	0.29	1.15 K	+0.11 K	0.29	1.22 K	+0.44 K
MULT	0.33	1.69 K	+1.25 K	0.33	1.72 K	+1.28 K	0.31	1.74 K	+1.26 K	0.35	1.88 K	+1.48 K
INT	0.45	1.02 K	+0.01 K	0.46	1.03 K	+0.08 K	0.47	1.04 K	+0.01 K	0.46	1.12 K	+0.28 K
Egelsee depression 2019												
ADD	0.00	1.54 K	+1.27 K	0.00	1.60 K	+1.32 K	0.00	1.54 K	+1.24 K	0.00	1.51 K	+1.21 K
MULT	0.00	1.61 K	+1.32 K	0.00	1.66 K	+1.36 K	0.00	1.61 K	+1.31 K	0.00	1.57 K	+1.27 K
INT	0.00	1.59 K	+1.27 K	0.00	1.64 K	+1.33 K	0.00	1.56 K	+1.24 K	0.00	1.53 K	+1.21 K

<https://doi.org/10.1371/journal.pclm.0000089.t007>

## Discussion

### Estimation of nocturnal air temperature variability using LUR models

The present study aims to model nocturnal UHI intensities and map summertime nighttime air temperatures in a city with complex terrain using a LUR approach, whereas three different model structures and four CAD variables are tested. Hereby, one crucial step is the selection of the critical meteorological and land use variables. It has been shown in various studies, that large UHI intensities are found during “calm and clear” (low wind speed and clear sky) nights after radiation intense days [4,18–21]. This research leads to similar findings for the city of Bern, but with the addition, that wind direction may also play an important role depending on the location of the rural reference station. Here, the rural reference station is located in the northeast of the city (Fig 1B), and if the winds originate from this direction, air masses close to the reference station were likely to be exchanged faster than in the city, due to blocking by buildings or orography. Hence, the temperature differences between urban sites and the rural reference station in Zollikofen are even larger during nights with northerly winds than during calm nights. Conversely, winds from southeast or southwest lead to strongly declining UHI intensities (Fig 3E). Additionally, little attention has so far been given to the inclusion of precipitation variables in similar LUR modeling studies, since the focus has mainly been on conditions favoring large UHI intensities [4,12,14]. However, the weakening effect of precipitation on the UHI intensity in general is well documented [19,22] and should be incorporated if longer timespans are investigated. Here, a Boolean precipitation variable instead of a numerical variable is used, which can be justified by the fact that precipitation events during the night likely vanishes a substantial share of the urban heat, independently of the amount of precipitation.

The land use variables that are significant in this study differ slightly from a previous study in the same city, which only focused on land use variables and heatwave episodes [17]. While the main pattern of open and vegetated areas having a cooling effect is similar, the cooling effect of forested areas and dense vegetation is more explicit in this study. Contrariwise, the cooling effect of water seems to be less pronounced if the entire summer is analyzed, which might be due to the water temperatures not significantly being cooler than the air temperatures during the night. Within the densely built areas, unsealed garden areas and vegetation lead to lower local temperatures (Figs 4 and S2–S9). Another important difference compared to the previous study is that altitude is directly incorporated in the model with the variable AD. This allows for a modeling of warm hilltops and slopes during calm and clear nights (Fig 4A, 4C and 4D), which is an important feature since such inversion patterns are a typical characteristic of the local climate of Bern [37]. However, when analyzing such rural, hilly areas, it is important to keep in mind that only a few rural stations were available for model calibration and validation, making uncertainties larger in these locations of the study area.

The evaluation with additional data (Table 6) shows that the model performance ( $R^2$  and RMSE) is similar (summer 2018) or a bit lower (summer 2021) compared to the calibration data (Table 4). The air temperatures are rather underestimated during 2018 (MB -0.21 to -0.29 K) and overestimated during 2021 (MB +0.41 to +0.43 K; Table 6). One likely reason for these differences can be found in the fact that Switzerland experienced a very hot and record dry summer 2018 and a rather cool and very wet summer 2021 [52,53]. The differences in air temperature and precipitation might thus have led to a very different state of the vegetation during these summers, having larger evaporative cooling capacities during summer 2021, which may have caused lower UHI intensities. In this study, the land use variables including vegetation are treated as static and thus do not account for changes due to inter-annual variability of meteorological background conditions. An inclusion of such an additional variable accounting

for the year to year changes in the state of the vegetation (e.g. NDVI) would be an interesting supplement for future studies.

The presented LUR models are subject to additional limitations being worthwhile to be mentioned. As such, shallow depressions may cause air temperature differences of several K during nighttime [25], even within a city. The application of the models on a shallow depression shows that none of the models is able to represent such small-scale air temperature differences in an adequate manner (Table 7). This might be due to the rather large buffer radii of the land use variables (up to 1000 m; Table 1) or the cooling effect of the CAD variables being too weak: A detailed analysis of the CAD variables shows that they are only able to capture about 0.6 K of the cooling in the Egelsee depression, whereas differences of up to 3 K are reached under favorable conditions. Another limitation is that the models tested here are static and do not take into account weather patterns from previous days and resulting variables depending on those, such as soil moisture, which may influence the present day air temperature patterns [20]. Lastly, the exposition of a location to the wind is not incorporated, since no land use variable was found which was able to represent this aspect.

### Differences between model structures and CAD variables

Three model structures with different degrees of complexity and four straight forward computable variables to incorporate cold air dynamics induced by topographic features are tested in this study. Regarding the model structures, the MULT models show inaccuracies if either a station is not considerably warmer (or even cooler) than the reference station, or if a day with meteorological conditions unfavorable for the formation of the UHI is modeled. In both cases, one of the factors in the equation of the MULT model is found to be close to zero or negative (Table 2), and the resulting variability of urban air temperatures is not realistic (Fig 3B). Hence, this model structure is only appropriate if “cool” reference and “warm” urban stations are used and only when days with meteorological conditions favoring large UHI intensities are analyzed. Besides that, enhanced complexity leads to better performance. The inclusion of the interaction terms leads to an increase in  $R^2$  between 0.057 and 0.058 (depending on the CAD variable), which implies that the interaction effect accounts for 5.7 to 5.8% of the variance [50]. In the simple ADD model, the magnitude and the shape of the UHI remains similar for every night (Fig 4A and 4B), whereas the effect of different meteorological conditions on the formation of urban heat islands (and also CAD) can be incorporated with the interaction terms.

The resulting air temperature fields of all CAD variables show more realistic patterns than the simple flow accumulation approach of an earlier study [17] (Figs 4 and S2–S9). The largest differences between the CAD variables can be found in areas where strong CAD is expected. While models based on elevation based CADs model the typical pattern of temperature inversions in a more pronounced way, flow accumulation based CADs are able to model cold air paths along the topography (Fig 5). Due to the limited number of stations in the hilly areas and the similar performance in calibration and evaluation, no statement about which CAD variable to be the most appropriate can be made here. Additionally, it has to be stated that none of the CAD variables is capable to model cooling effects of a small-scale depression within the city (Table 7), and that potential blocking effects of buildings or trees are not incorporated by three out of four CAD variables (FA, TPI and REH). Additional research and the evaluation of these CAD variables in other cities with complex terrain would hence be beneficial.

### Conclusions

The aim of this study was to model nocturnal UHI intensities and to map nighttime air temperature fields in the city of Bern during summers 2018 to 2020 with a LUR approach based

on air temperature data of a low cost measurement network and publicly available geospatial and meteorological data.

The results show that, in addition to precipitation, global solar radiation and wind speed, wind direction is an important factor for the distribution of the nocturnal urban air temperatures variability in Bern. Further, we tested three different model structures to combine meteorology and land use and four straight-forward computable variables to predict cold air drainage. The resulting 12 models reached good model performances ( $R^2$  0.65 to 0.71; RMSE 0.69 to 0.76) which could be validated with additional data ( $R^2$  0.59 to 0.73; RMSE 0.77 to 0.85). While multiplicative model structures were not able to realistically predict the air temperatures of cool stations and for days with meteorological conditions unfavorable for the formation of urban heat, additive and integrative model structures performed well, of which the latter is favored due to the possibility of modeling different magnitudes of urban heat island intensity.

With the derived models, it is possible to calculate and map the air temperature distribution of a city in complex terrain for every night of a summer using meteorological data of only one official measurement station and publicly available land use data. With this method, only a very low amount of computational (about 5 min on a basic computer for 92 days) and financial (publicly available data) effort is needed to gain valuable information about the intra-urban temperature distribution in a city which can then be used for various applications in urban planning, heat risk management and future research.

## Supporting information

**S1 Fig. Predicted (x-axis) versus measured UHI intensities of all 12 models.**  
(TIF)

**S2 Fig.** Predicted mean nighttime air temperatures derived from the ADD (A and B), MULT (C and D) and INT models (E and F) with the CAD variable FA for the 5<sup>th</sup> of August 2018 (A, C and E) and the 9<sup>th</sup> of August 2019 (B, D and E). The dots show measured mean nighttime air temperatures of the correspondent night at the sites used for the modeling. The model performance is indicated by the correlation ( $r$ ), the root mean square error (RMSE) and the mean bias (MB). The base layer (building shadows) can be downloaded using the following link: <https://www.swisstopo.admin.ch/en/geodata/landscape/buildings3d2.html>.  
(TIF)

**S3 Fig.** Predicted mean nighttime air temperatures derived from the ADD (A and B), MULT (C and D) and INT models (E and F) with the CAD variable FAB for the 5<sup>th</sup> of August 2018 (A, C and E) and the 9<sup>th</sup> of August 2019 (B, D and E). The dots show measured mean nighttime air temperatures of the correspondent night at the sites used for the modeling. The model performance is indicated by the correlation ( $r$ ), the root mean square error (RMSE) and the mean bias (MB). The base layer (building shadows) can be downloaded using the following link: <https://www.swisstopo.admin.ch/en/geodata/landscape/buildings3d2.html>.  
(TIF)

**S4 Fig.** Predicted mean nighttime air temperatures derived from the ADD (A and B), MULT (C and D) and INT models (E and F) with the CAD variable REH for the 5<sup>th</sup> of August 2018 (A, C and E) and the 9<sup>th</sup> of August 2019 (B, D and E). The dots show measured mean nighttime air temperatures of the correspondent night at the sites used for the modeling. The model performance is indicated by the correlation ( $r$ ), the root mean square error (RMSE) and the mean bias (MB). The base layer (building shadows) can be downloaded using the following



link: <https://www.swisstopo.admin.ch/en/geodata/landscape/buildings3d2.html>.  
(TIF)

**S5 Fig. High resolution maps of the Flow Accumulation (FA) interaction models for the 5<sup>th</sup> of August 2018 and the 9<sup>th</sup> of August 2019.** The colored dots show the model stations with the measured mean nighttime air temperatures of the correspondent night. The base layer (building shadows) can be downloaded using the following link: <https://www.swisstopo.admin.ch/en/geodata/landscape/buildings3d2.html>.  
(JPG)

**S6 Fig. High resolution maps of the Flow Accumulation with Buildings (FAB) interaction models for the 5<sup>th</sup> of August 2018 and the 9<sup>th</sup> of August 2019.** The colored dots show the model stations with the measured mean nighttime air temperatures of the correspondent night. The base layer (building shadows) can be downloaded using the following link: <https://www.swisstopo.admin.ch/en/geodata/landscape/buildings3d2.html>.  
(JPG)

**S7 Fig. High resolution maps of the Topographic Position Index (TPI) interaction models for the 5<sup>th</sup> of August 2018 and the 9<sup>th</sup> of August 2019.** The colored dots show the model stations with the measured mean nighttime air temperatures of the correspondent night. The base layer (building shadows) can be downloaded using the following link: <https://www.swisstopo.admin.ch/en/geodata/landscape/buildings3d2.html>.  
(JPG)

**S8 Fig. High resolution maps of the Relative Height (REH) interaction models for the 5<sup>th</sup> of August 2018 and the 9<sup>th</sup> of August 2019.** The colored dots show the model stations with the measured mean nighttime air temperatures of the correspondent night. The base layer (building shadows) can be downloaded using the following link: <https://www.swisstopo.admin.ch/en/geodata/landscape/buildings3d2.html>.  
(JPG)

**S9 Fig.** Predicted mean nighttime air temperatures derived from the INT models with the CAD variables FA (A and B), FAB (C and D), TPI (E and F), and REH (G and H) for the 5<sup>th</sup> of August 2018 (A, C, E, and G) and the 9<sup>th</sup> of August 2019 (B, D, E, and H). The colored dots show the model stations with the measured mean nighttime air temperatures of the correspondent night. The model performance is indicated by the correlation (r), the root mean square error (RMSE) and the mean bias (MB). The base layer (building shadows) can be downloaded using the following link: <https://www.swisstopo.admin.ch/en/geodata/landscape/buildings3d2.html>.  
(TIF)

**S10 Fig. Deviations in predicted mean nighttime air temperatures between the four different Cold Air Drainage (CAD) Interaction models for the 9<sup>th</sup> of August 2019.** The abbreviations stand for the different CAD proxies: REH = Relative Height; TPI = Topographic Position Index; FA = Flow Accumulation; FAB = Flow Accumulation with Buildings. The base layer (building shadows) can be downloaded using the following link: <https://www.swisstopo.admin.ch/en/geodata/landscape/buildings3d2.html>.  
(TIF)

**S1 Table. Resulting models with the CAD variable FA.**  
(PDF)

**S2 Table. Resulting models with the CAD variable FAB.**  
(PDF)

**S3 Table. Resulting models with the CAD variable TPI.**  
(PDF)

## Acknowledgments

We thank Saba Baer, André Hürzeler and Lukas Meyer for their help of setting up and maintaining the measurement network as well as a variety of local stakeholders (city of Bern and communities of Köniz and Ostermundigen, Tiefbauamt Bern, Energie Wasser Bern, Bernmobil, BKW Energie AG, Burgergemeinde Bern, Energie Belp, Stadtgrün Bern, Meteoschweiz, SBB, Amt für Umwelt und Sportplatz, Viererfeld, Gurtenbahn Bern AG) for the permission to use their infrastructure for the deployment of our measurement stations. We also thank Peter Leiser for his support regarding various technical challenges, which arose during the fieldwork and Christoph von Matt for his valuable hints regarding coding in R.

## Author Contributions

**Conceptualization:** Moritz Burger, Moritz Gubler, Stefan Brönnimann.

**Data curation:** Moritz Burger.

**Formal analysis:** Moritz Burger.

**Funding acquisition:** Stefan Brönnimann.

**Methodology:** Moritz Burger.

**Project administration:** Moritz Burger.

**Software:** Moritz Burger.

**Supervision:** Moritz Gubler, Stefan Brönnimann.

**Validation:** Moritz Burger.

**Visualization:** Moritz Burger.

**Writing – original draft:** Moritz Burger.

**Writing – review & editing:** Moritz Burger, Moritz Gubler, Stefan Brönnimann.

## References

1. EEA (European Environment Agency). Climate change, impacts and vulnerability in Europe 2016. An indicator-based report. 2017; Luxembourg, 424 pp. ISBN 978-92-9213-835-6.
2. EEA (European Environment Agency). Europe's changing climate hazards—an index-based interactive EEA report. 2021; Report no. 15/2021. HTML—TH-AL-21-015-EN-Q- ISBN 978-92-9480-407-5 ISSN 1977-8449—<https://doi.org/10.2800/458052>
3. Oke TR, Mills G, Christen A, Voogt JA. Urban climates. Cambridge University Press. 2017.
4. Theeuwes NE, Steeneveld GJ, Ronda RJ, Holtslag AA. A diagnostic equation for the daily maximum urban heat island effect for cities in northwestern Europe. *International Journal of Climatology*, 2017; 37(1), 443–454.
5. Köllner P, Gross C, Schächli B, Füssler J, Lerch J, Nauser M. Klimabedingte Risiken und Chancen. Eine schweizweite Synthese. (EN: "Climate-related risks and opportunities. A Switzerland-wide synthesis."). Bundesamt für Umwelt (BAFU)—Federal Office for the Environment (FOEN), Bern. 2017. Umwelt-Wissen Nr. 1706: 148 S.
6. Muller CL, Chapman L, Grimmond CSB, Young DT, Cai X. Sensors and the city: a review of urban meteorological networks. *International Journal of Climatology*, 2013; 33(7), 1585–1600.

7. Gehrig R, König N, Scherrer S. Städtische Wärmeinsel in der Schweiz—Klimatologische Studie mit Messdaten in fünf Städten (EN: “Urban Heat Islands in Switzerland—Climatological study with measured data from five cities”), Fachbericht MeteoSchweiz, 2018; 273, 61 pp.
8. Liu L, Zhang Y. Urban heat island analysis using the Landsat TM data and ASTER data: A case study in Hong Kong. *Remote sensing*, 2011; 3(7), 1535–1552.
9. Schwaab J, Meier R, Mussetti G, Seneviratne S, Bürgi C, Davin EL. The role of urban trees in reducing land surface temperatures in European cities. *Nature communications*, 2021; 12(1), 1–11.
10. Holec J, Feranec J, Šťastný P, Szatmári D, Kopecká M, Garaj M. Evolution and assessment of urban heat island between the years 1998 and 2016: case study of the cities Bratislava and Trnava in western Slovakia. *Theoretical and Applied Climatology*, 2020; 141(3), 979–997.
11. Hollósi B, Žuvela-Aloise M, Oswald S, Kainz A, Schöner W. Applying urban climate model in prediction mode—evaluation of MUKLIMO\_3 model performance for Austrian cities based on the summer period of 2019. *Theoretical and Applied Climatology*, 2021; 144(3), 1181–1204.
12. Ali JM, Marsh SH, Smith MJ. Modelling the spatiotemporal change of canopy urban heat islands. *Building and Environment*, 2016; 107, 64–78.
13. Foissard X, Dubreuil V, Quénot H. Defining scales of the land use effect to map the urban heat island in a mid-size European city: Rennes (France). *Urban Climate*, 2019; 29, 100490.
14. Chen YC, Liao YJ, Yao CK, Honjo T, Wang CK, Lin TP. The application of a high-density street-level air temperature observation network (HiSAN): The relationship between air temperature, urban development, and geographic features. *Science of the Total Environment*, 2019; 685, 710–722. <https://doi.org/10.1016/j.scitotenv.2019.06.066> PMID: 31234133
15. Sera F, Armstrong B, Tobias A, Vicedo-Cabrera AM, Åström C, Bell ML, et al. How urban characteristics affect vulnerability to heat and cold: a multi-country analysis. *International journal of epidemiology*, 2019; 48(4), 1101–1112. <https://doi.org/10.1093/ije/dyz008> PMID: 30815699
16. Huang KT, Hwang RL. Future trends of residential building cooling energy and passive adaptation measures to counteract climate change: The case of Taiwan. *Applied Energy*, 2016; 184, 1230–1240.
17. Burger M, Gubler M, Heinemann A, Brönnimann S. Modelling the spatial pattern of heatwaves in the city of Bern using a land use regression approach. *Urban climate*, 2021; 38, 100885.
18. Morris C, Simmonds I, Plummer N. Quantification of the influences of wind and cloud on the nocturnal urban heat island of a large city. *Journal of Applied Meteorology and Climatology*, 2001; 40(2), 169–182.
19. Runnalls KE, Oke TR. Dynamics and controls of the near-surface heat island of Vancouver, British Columbia. *Physical Geography*, 2000; 21(4), 283–304.
20. Kim YH, Baik JJ. Daily maximum urban heat island intensity in large cities of Korea. *Theoretical and Applied Climatology*, 2004; 79(3), 151–164.
21. Hoffmann P, Krueger O, Schlünzen KH. A statistical model for the urban heat island and its application to a climate change scenario. *International Journal of Climatology*, 2012; 32(8), 1238–1248.
22. He BJ. Potentials of meteorological characteristics and synoptic conditions to mitigate urban heat island effects. *Urban climate*, 2018; 24, 26–33.
23. Mathys H, Maurer R, Messerli B, Wanner H, Winiger M. Klima und Luft hygiene im Raum Bern. Resultate des Forschungsprogrammes KLIMUS und ihre Anwendung in der Raumplanung. (EN: “Climate and air pollution control in the area of Bern. Results of the KLIMUS research program and the application in urban planning”) Schweizerische Naturforschende Gesellschaft, 1980; (7).
24. Grunwald L, Kossmann M, Weber S. Mapping urban cold-air paths in a Central European city using numerical modelling and geospatial analysis. *Urban Climate*, 2019; 29, 100503.
25. Mahrt L, Vickers D, Nakamura R, Soler MR, Sun J, Burns S, et al. Shallow drainage flows. *Boundary-layer meteorology*, 2001; 101(2), 243–260.
26. Buttstädt M, Schneider C. Thermal load in a medium-sized European city using the example of Aachen, Germany. *Erdkunde*, 2014; 71–83.
27. Wicki A, Parlow E, Feigenwinter C. Evaluation and modeling of urban heat island intensity in Basel, Switzerland. *Climate*, 2018; 6(3), 55.
28. Shi Y, Katzschne L, Ng E. Modelling the fine-scale spatiotemporal pattern of urban heat island effect using land use regression approach in a megacity. *Science of the Total Environment*, 2018; 618, 891–904. <https://doi.org/10.1016/j.scitotenv.2017.08.252> PMID: 29096959
29. Suder A, Szymanowski M. Determination of ventilation channels in urban area: a case study of Wrocław (Poland). *Pure and Applied Geophysics*, 2014; 171(6), 965–975.

30. Chung U, Seo HH, Hwang KH, Hwang BS, Choi J, Lee JT, et al. Minimum temperature mapping over complex terrain by estimating cold air accumulation potential. *Agricultural and Forest Meteorology*, 2006; 137(1–2), 15–24.
31. Bennie JJ, Wiltshire AJ, Joyce AN, Clark D, Lloyd AR, Adamson J, et al. Characterising inter-annual variation in the spatial pattern of thermal microclimate in a UK upland using a combined empirical–physical model. *Agricultural and Forest Meteorology*, 2010; 150(1), 12–19.
32. Ashcroft MB, Gollan JR. Fine-resolution (25 m) topoclimatic grids of near-surface (5 cm) extreme temperatures and humidities across various habitats in a large (200× 300 km) and diverse region. *International Journal of Climatology*, 2012; 32(14), 2134–2148.
33. Bigg GR, Wise SM, Hanna E, Mansell D, Bryant RG, Howard A. Synoptic climatology of cold air drainage in the Derwent Valley, Peak District, UK. *Meteorological Applications*, 2014; 21(2), 161–170.
34. Grunwald L, Schneider AK, Schroeder B, Weber S. Predicting urban cold-air paths using boosted regression trees. *Landscape and Urban Planning*, 2020; 201, 103843.
35. Gubler M, Christen A, Remund J, Brönnimann S. Evaluation and application of a low-cost measurement network to study intra-urban temperature differences during summer 2018 in Bern, Switzerland. *Urban climate*, 2021; 37, 100817.
36. BFS (Bundesamt für Statistik), SSV (Schweizerischer Städteverband). Statistik der Schweizer Städte 2021—Statistiques des villes suisse 2021 (EN: “Statistics of the Swiss cities 2021”). 00 Statistische Grundlagen und Übersichten. 2021; Neuchâtel, Bern.
37. Mathys H. Die Temperaturverhältnisse in der Region Bern (EN: “The temperature conditions in the bern region”). Beiträge zum Klima der Region Bern. 1976; Beitrag No. 3. Geographisches Institut der Universität Bern. Bern.
38. MeteoSwiss. Klimanormwerte Bern/Zollikofen, Normperiode 1981–2010. (EN: “Climate Normals Bern/Zollikofen, Normperiod 1981–2010”). Federal Office of Meteorology and Climatology, 2020; Zurich.
39. WMO (World Meteorological Organization) Guide to Meteorological Instruments and Methods of Observation. WMO-Nr. 8. 2008; Geneva, Switzerland. ISBN: 978-92-63-100085.
40. MeteoSwiss. IDAWEB. [www.gate.meteoswiss.ch/idaweb/login.do?language=en](http://www.gate.meteoswiss.ch/idaweb/login.do?language=en) (last access: 09/15/2022).
41. Amt für Geoinformation des Kantons Bern. Amtliche Vermessung vereinfacht (EN: “Cadastral survey simplified”) (MOPUBE). 2021; Dataset. Available from: <https://www.agi.dij.be.ch/de/start/geoportal/geodaten/geodaten-zum-download/geoprodukte-zum-download.html>.
42. Swisstopo (Federal Office of Topography). swissALTI3D. 2020; Dataset. Available from: <https://www.swisstopo.admin.ch/en/geodata/height/alti3d.html>.
43. Swisstopo (Federal Office of Topography). swissTLM3D. 2021; Dataset. Available from: <https://www.swisstopo.admin.ch/en/geodata/landscape/tlm3d.html>.
44. Ginzler C, Hobi ML. Countrywide stereo-image matching for updating digital surface models in the framework of the Swiss National Forest Inventory. *Remote Sensing*, 2015; 7(4), 4343–4370.
45. Swisstopo (Federal Office of Topography). swissBUILDINGS3D 2.0. 2021; Dataset. Available from: <https://www.swisstopo.admin.ch/en/geodata/landscape/buildings3d2.html>.
46. ESRI. Arc Gis. Version 10.7. Release Date March 21, 2019.
47. Jenson SK, Domingue JO. Extracting topographic structure from digital elevation data for geographic information system analysis. *Photogrammetric engineering and remote sensing*, 1988; 54(11), 1593–1600.
48. Hoek G, Beelen R, De Hoogh K, Vienneau D, Gulliver J, Fischer P, et al. A review of land-use regression models to assess spatial variation of outdoor air pollution. *Atmospheric environment*, 2008; 42(33), 7561–7578.
49. Stewart ID, Oke TR. Local climate zones for urban temperature studies. *Bulletin of the American Meteorological Society*, 2012; 93(12), 1879–1900.
50. Jaccard J, Turrisi R. Interaction Effects in Multiple Regression (2<sup>nd</sup> ed). Sage University Paper Series on Quantitative Applications in the Social Sciences, 2003; 07–072. Thousand Oaks, CA: Sage.
51. R Core Team. R: A language and environment for statistical computing. R Foundation for Statistical Computing, 2019; Vienna, Austria. URL: <https://www.R-project.org/>.
52. MeteoSwiss. Klimabulletin Sommer 2018 (EN: “Climate report of the summer 2018”). 2018; Zurich.
53. MeteoSwiss. Klimabulletin Sommer 2021 (EN: “Climate report of the summer 2021”). 2021; Zurich.